

The role of surface substitution in the atomic disorder-to-order phase transition in multi-component core–shell structures

Received: 5 December 2023

Accepted: 1 November 2024

Published online: 11 November 2024

 Check for updates

Wencong Zhang^{1,2}, Fan Li¹, Yi Li^{1,2}, Anran Song^{1,2}, Kun Yang^{1,2}, Dongchang Wu³, Wen Shang¹, Zhenpeng Yao^{1,2,4}✉, Wenpei Gao^{1,2,4}✉, Tao Deng¹ & Jianbo Wu^{1,2,4}✉

Intermetallic phases with atomic ordering are highly active and stable in catalysts. However, understanding the atomistic mechanisms of disorder-to-order phase transition, particularly in multi-component systems, remains challenging. Here, we investigate the atom diffusion and phase transition within Pd@Pt-Co cubic nanoparticles during annealing, using in-situ electron microscopy and ex-situ atomic resolution element analysis. We reveal that initial outward diffusing Pd partially substitutes Pt, forming a (Pt, Pd)-Co ternary system in the surface region, enabling the phase transition at a low temperature of 400 °C, followed by shape-preserved inward propagation of the ordered phase. At higher temperatures, excessive interdiffusion across the interface changes the stoichiometric ratio, diminishing the atomic ordering, leading to obvious change in morphology. Calculations indicate that the Pd-substitute in (Pt, Pd)-Co system leads to a significantly lower phase transition temperature compared to that of Pt-Co alloy and thus a lower activation energy for atomic diffusion. These insights into atomistic behavior are crucial for future design of multi-component systems.

Pt-based catalysts play a vital role in electrocatalysis, particularly, the oxygen reduction reaction (ORR) in proton-exchange membrane fuel cells (PEMFCs)^{1–5}. However, the high cost and limited availability of Pt greatly hinder the commercial application of fuel cells^{1,2,6}. Alloying Pt with other metals to form binary, ternary, and even high-entropy alloys has been developed to obtain cost-effective Pt-based catalysts with improved activity^{7–11}. To further maximize the utilization of Pt, shape-controlled core–shell nanoparticles (NPs), with non-Pt metals in the core and Pt or Pt-based alloy on the shell, have been synthesized^{12–14}. Among the core–shell NPs, Pd has been identified as an ideal core due to its negligible lattice mismatch with Pt (0.77%)^{12,13,15}. Shape-controlled Pd@Pt/Pt-based alloy NPs have demonstrated enhanced catalytic activity in numerous studies^{12–15}. However, corrosion of atoms in the

shell during the long-term durability test always leads to the loss of designed morphology, composition distribution, and structure, resulting in severe activity degradation^{13,16,17}. In contrast, the intermetallic phase exhibits improved stability under harsh acidic environments compared to their alloy counterparts, which is ascribed to their lower enthalpy and increased strength of the periodic heteroatomic bonding¹⁸. Thus, forming an ordered structure at the surface of core–shell NPs is anticipated to improve both catalytic activity and stability. However, the reported disorder-to-order phase transition of Pt-based alloys typically occurs at elevated temperatures, which often leads to the loss of well-defined facets^{5,19–22}. It is also observed that the ordered phase in multi-component systems retains the crystallographic structure of the binary counterparts^{23,24}. For core–shell

¹Center of Hydrogen Science & State Key Laboratory of Metal Matrix Composites, School of Materials Science and Engineering, Shanghai Jiao Tong University, Shanghai, People's Republic of China. ²Future Material Innovation Center, Zhangjiang Institute for Advanced Study, Shanghai Jiao Tong University, Shanghai, People's Republic of China. ³Shanghai Nanoport, Thermo Fisher Scientific, Shanghai, People's Republic of China. ⁴Materials Genome Initiative Center, Shanghai Jiao Tong University, Shanghai, People's Republic of China. ✉e-mail: z.yao@sjtu.edu.cn; gaowenpei@sjtu.edu.cn; jianbowu@sjtu.edu.cn

nanostructures, preserving the initial morphology and the core–shell interface during annealing at high temperatures is challenging^{25,26}, because of the tendency of shape reconstruction and the diffusion of elements in the core and shell^{26–28}. Therefore, it is critical to initiate the disorder-to-order phase transition at low annealing temperatures, contributing to the preservation of surface and interface integrity^{29,30}.

To elucidate the underlying mechanism of ordering conversion, in-situ transmission electron microscopy (TEM) has been applied to monitor the atomic motion in nanomaterials under reactive environments^{22,31–33}. We have revealed that the ordering process for Pt₃Co cubes annealed at 600–700 °C starts from the surface, and the ordered nuclei grow inwards following a layer-by-layer process³⁴. The final structure and morphology of Pt₃Co cubes are determined by the competition between surface diffusion and phase transition during annealing. In Pt–Fe nanoalloys, works show that the disorder-to-order transition at 700 °C strongly depends on the alloy composition. Pt₈₅Fe₁₅ adopts the “nucleation and growth” mechanism and has an L1₂-ordered core, while Pt₆₅Fe₃₅ follows the “interface” mechanism, resulting in an L1₀ core³⁵. However, most of the reported in-situ disorder-to-order transitions have been conducted at high temperatures and are limited to uniform binary alloy systems^{20,31,36}. Understanding atomic diffusion during in-situ observations of multi-component systems remains a challenge due to their structural and compositional complexity. To clarify the atom behaviors in different regions of the core–shell NPs, the concepts of Hüttig temperature (T_H), associated with surface-atom activation, and Tammann temperature (T_T), corresponding to the diffusion of interior atoms^{37,38}, have been introduced to explore the potential of low-temperature annealing treatments. Both T_H and T_T are determined by the melting point and strongly influenced by the size and composition of nanomaterials^{39,40}. By optimizing the design of nanomaterials, it is possible to trigger atomic migration at a “lower temperature” threshold that surpasses both the T_H and T_T . Direct observation of the atomic diffusion can reveal its correlation with the disorder-to-order phase transition and shape changes.

In this study, we investigated Pd@Pt-Co cubic NPs (≈ 13 nm) to study the phase transition at low temperatures and with a focus on the

atomic scale evolution of different phases in regions of nm in length scale. Previous works show that the cubic NPs with an average size of 10–15 nm are well-suited for tracking structural evolution over time using in-situ electron microscopy^{31,34,35}. With the Pd@Pt-Co cubic NPs, results show the outward diffusing Pd partially substitutes Pt atoms, forming a ternary (Pd, Pt)-Co system in the shell region, where the ordering transition occurs at significantly lower annealing temperatures. This ordered structure progressively propagates along the surface and extends into the NP core while preserving the surface orientation. At higher annealing temperatures, the cubic morphology and the pristine core–shell interface gradually disappear due to the excessive atomic diffusion, which also results in the loss of stoichiometric atomic ratio of the ordered phase. This indicates there is a critical temperature and time window in the annealing process for the surface-ordered structure to form while retaining the specific facets of the NPs. Additionally, theoretical calculation reveals that Pd-substituted (Pt, Pd)-Co composition underlies a lower phase-transition temperature (T_C) compared to binary Pt-Co alloy, which allows the formation of an L1₂-ordered surface in the cubic core–shell NPs. By correlating transition kinetics with chemical composition, we unveil the details involved in ordering transition for ternary core–shell NPs, providing insights into the rational design of Pt-based multi-component electrocatalysts.

Results

Insights into the Pd@Pt-Co core–shell cubes at atomic scale

Pd@Pt-Co core–shell cubes were synthesized through a typical seed-mediated approach, in which Pd cubic NPs with an average size of 10.2 ± 0.87 nm served as seeds for the conformal deposition of Pt and Co atoms (Supplementary Fig. 1). Figure 1a presents the high-angle annular dark-field scanning TEM (HAADF-STEM) image at low magnification of obtained Pd@Pt-Co NPs, which exhibits a uniform size distribution of 13.0 ± 1.02 nm and well-defined cubic morphology (Supplementary Fig. 2). The aberration-corrected STEM (AC-STEM) image of an individual Pd@Pt-Co NP (Fig. 1b) shows a clear Z-contrast difference between core and shell, originating from the different atomic numbers of Pd, Pt, and Co. According to the energy dispersive X-ray

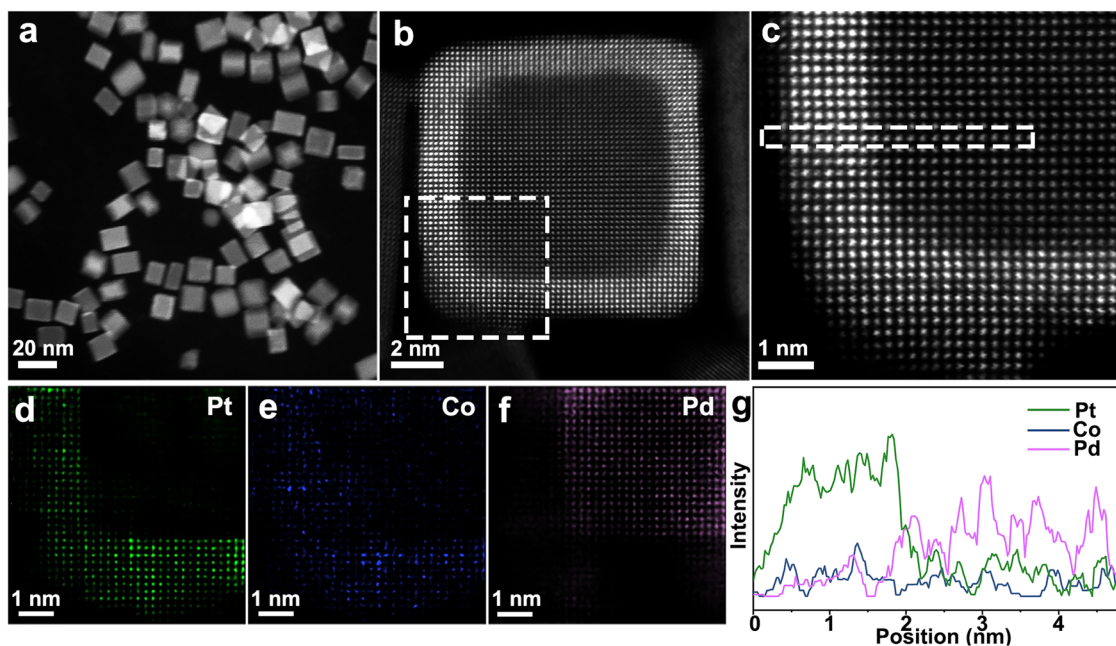


Fig. 1 | Structural and compositional analysis of pristine Pd@Pt-Co core–shell cubes. **a** Low-magnification HAADF-STEM image showing the cubic shape and good uniformity of the NPs. **b** Atomic resolution STEM image of an individual NP showing the apparent core–shell structure. **c** Enlarged region of NP

marked by white dotted box in **(b)**. **d–f** Atomic resolution EDS elemental mapping of Pt **(d)**, Co **(e)**, and Pd **(f)** derived from the enlarged region selected by the white dotted box in **(b)**. **g** Line scanning profile taken along the white dotted box in **(c)**. Source data are provided as a Source Data file.

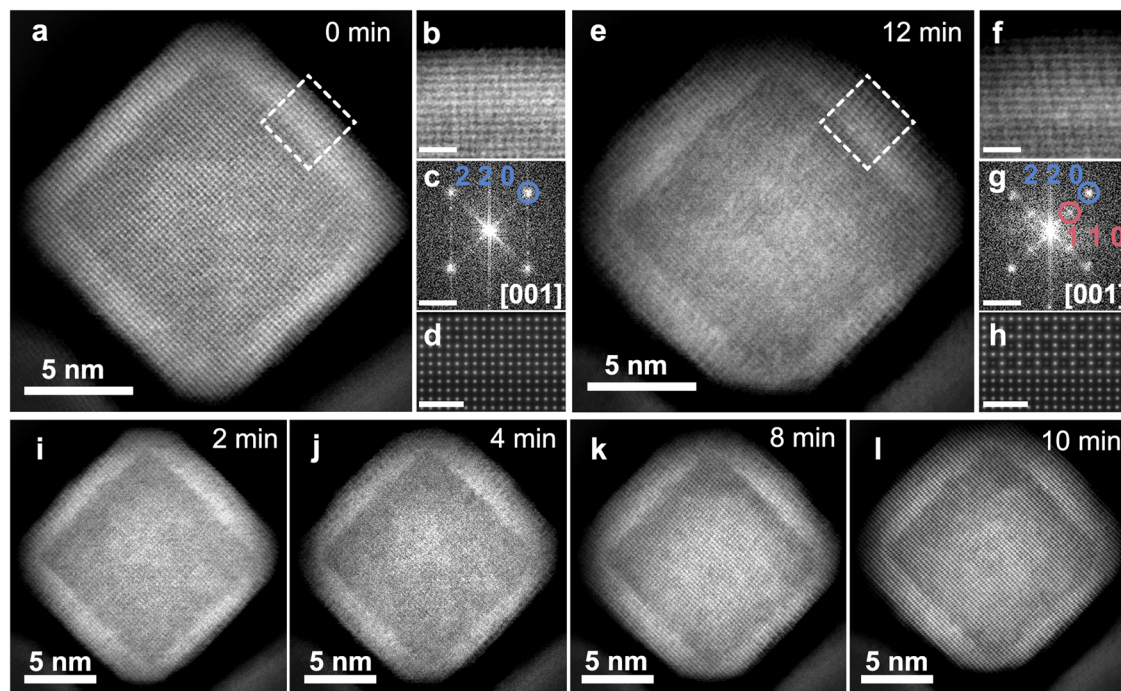


Fig. 2 | Sequential HAADF-STEM images of the Pd@Pt-Co cubes annealed at 400 °C in vacuum. a–h STEM images, enlarged view of the region marked by dashed white boxes (scale bar in (b, f) is 1 nm), corresponding FFT pattern (scale bar in (c, g) is 5 nm^{-1}), and simulated HAADF-STEM images (scale bar in (d, h) is 1 nm) of pristine Pd@Pt-Co NP (a–d) and Pd@Pt-Co NP annealed for 12 min (e–h) (see

Supplementary Figs. 4, 5 for the details of multi-slice simulation process). The blue and pink circles, and corresponding text refer to the diffraction features of disordered and ordered phases, respectively. i–l, Series of STEM images acquired at 2, 4, 8, and 10 min, respectively.

spectroscopy (EDS) analysis (Supplementary Fig. 3), the observed peaks of Pd, Pd, and Co prove the co-existence of the three elements. To further study the elemental distribution, the EDS mapping of Pd, Pt, and Co at an atomic resolution was conducted and presented (Fig. 1d–f). The line scanning profiles (Fig. 1g) extracted from the dotted box in Fig. 1c, further confirming the successful deposition of the Pt-Co shell on the Pd core.

In-situ tracking the atom diffusion

To explore the possibility of disorder-to-order transition at low temperatures for Pd@Pt-Co cubic NPs, the in-situ TEM technique was applied to track the structural changes of selected NPs annealing at 400 °C under vacuum. Figure 2 presents the sequential STEM images of the Pd@Pt-Co cubes during annealing, projected along the zone axis of [001]. As shown in Fig. 2a, the core-shell NP exhibited well-exposed (100) facets when the annealing process started ($t=0$ min). An enlarged view of the region marked by the white dotted box in the NP is also displayed (Fig. 2b). In the fast Fourier transform (FFT) of the magnified area, the absence of (100) and (110) reflection indicates the disordered phase (Fig. 2c). The uniform Z contrast is comparable to the simulated STEM image of the surface region with a disordered Pt₃Co phase (Fig. 2d). The disorder-to-order phase transition starts as the sample is heated at 400 °C. After 12 min of heating, a contrast from an ordered phase is seen (Fig. 2e, f). The (110) superlattice spots in FFT pattern of particle further indicate a Pt₃Co L1₂ phase, which features with one dark column and surrounding eight bright columns along [001] direction in the simulated STEM image (Fig. 2g, h).

As for the concrete phase transition process, we found the L1₂ phase preferentially nucleates at the surface. With the prolongation of the annealing time, the as-formed ordered domains gradually coalesce and grow toward the bulk (Fig. 2i–l). Together with the surface phase evolution, we noted that the cubic morphology also exhibits delicate change, but the core-shell structure is always stable and prominent. According to the typical phase transition process, the ordered

structure is thermally stable at low temperatures, meaning that the metastable A1 phase tends to transit to the intermetallic L1₂ phase (Supplementary Fig. 6). Thus, the final realization of the low-temperature phase transition tightly depends on the energy barrier that atoms need to overcome to achieve the rearrangements. It is reported that the nanocrystals with large surface-to-volume ratios have lower disorder-to-order phase transition temperatures than the bulk system, making ordering conversion at low temperatures possible^{18,41,42}. Furthermore, the vibrant surface atoms with low coordination numbers also contribute to activating the atom rearrangement at the nanoscale region³⁴. Thus, both the size effect and sensitive surface response work together, making the ordering process happen at temperatures below T_c . However, previous studies found the ordering transition of Pt-based binary system typically occurs at higher temperatures than 600 °C^{5,43}. In this case, further investigation needs to be conducted to explain this unexpected nucleation at 400 °C occurring in Pd@Pt-Co cubes.

To further elucidate the growth of ordered structure, a continuous in-situ heating was imposed on Pd@Pt-Co cubes, during which the surface/interface evolutions determined by atomic diffusion were recorded. Specifically speaking, the surface/interface traces encompass the outline of cubic NP, the interface between core and shell, and the development of the ordered intermetallic phase. To establish a proof-of-concept initial state, the Pd@Pt-Co cube annealed at 445 °C was selected, building upon the nucleation of the ordered structure at 400 °C. In this case, the atom motions were accelerated by increasing annealing temperatures, leading to a more discernible structural transformation. STEM images acquired at a series of temperatures indicate that, as the annealing temperature increases, the sharp corner feature of the cubic morphology and the original core-shell interface gradually fade away (Fig. 3a, d, g, j, m, p). Remarkably, the multi-component Pd@Pt-Co core-shell NPs exhibit an accelerated rate of shape transformation concerning Pt-Co binary cubes previously reported, indicating the enhanced mobility of surface atoms within the

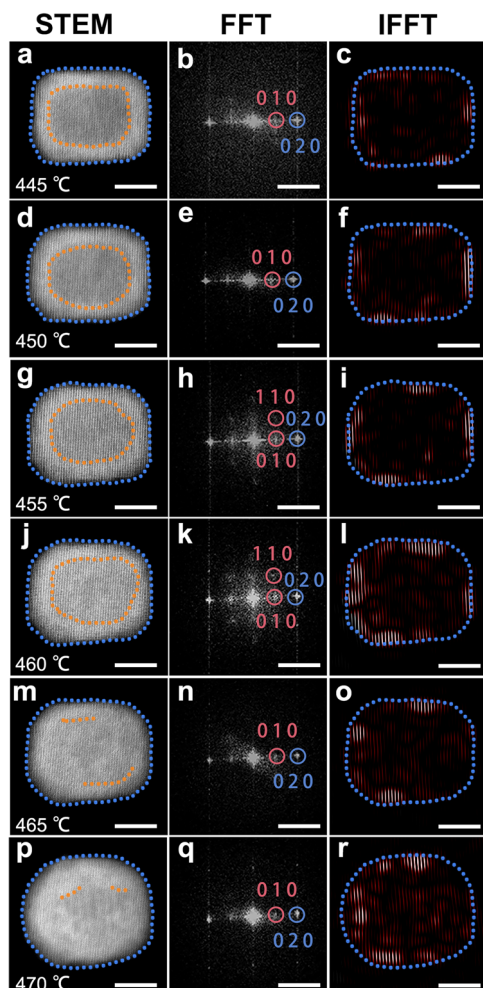


Fig. 3 | Dynamical evolution of an individual Pd@Pt-Co cube during in-situ heating. **a–r** Sequential HAADF-STEM images (scale bar in **(a, d, g, j, m, p)** is 5 nm), corresponding FFT patterns (scale bar in **(b, e, h, k, n, q)** is 5 nm^{-1}), and inverse FFT images (scale bar in **(c, f, i, l, o, r)** is 5 nm) derived from the superlattice spots marked with pink circles in FFT images were acquired at 445 °C (**a–c**), 450 °C (**d–f**), 455 °C (**g–i**), 460 °C (**j–l**), 465 °C (**m–o**), and 470 °C (**p–r**), respectively. The blue dashed lines mark the outline of the NP, and the orange lines mark the interface between the core and shell. The blue and pink circles, and corresponding text refer to the diffraction features of disordered and ordered phases, respectively. The pink regions in IFFT images indicate the ordered structure, where the color scale originates from the amount of ordered structure.

Pd@Pt-Co system³⁴. Meanwhile, at temperatures approaching 470 °C, distinguishing the core–shell interface becomes challenging due to temperature-promoted atomic interdiffusion motions driven by composition gradient within the core–shell NP.

Considering the thermal perturbations during in-situ observation, inverse fast Fourier transform (IFFT) patterns were performed to better visualize the growth behavior of the ordered structure based on the FFT-filtered results (Fig. 3b, e, h, k, n, q). The pink-tinted regions in resulting IFFT images correspond to the distribution of ordered structures (Fig. 3c, f, i, l, o, r), revealing that the growth of intermetallic adopts coalescence and inward extension manner in this case. The intermetallic phase primarily dominates and nucleates at the surface region during the in-situ annealing process, likely due to the limitation of chemical components. Additionally, the growth of the ordered structure is accompanied by multi-site nucleation, which differs from the “layer-by-layer” mode in the Pt-Co system reported in ref. 34. We also observed the intensity fluctuation in the FFT-filtered images, particularly the less ordered features in Fig. 3n compared to Fig. 3k. In contrast to the clear atomic columns in

Fig. 3j, more lattice fringes are observed in Fig. 3m, which is likely due to the rotation of NPs along the vertical direction during in-situ heating. To verify the inward growth of the ordered structure and study the effect of temperature on structural evolution, we performed additional ex-situ experiments. Pd@Pt-Co NPs were annealed at 450 and 650 °C, respectively. Consistent with in-situ observations, annealing at 450 °C resulted in an extended ordered region (Supplementary Fig. 7). While the ordered region is rarely left upon annealing of the NPs at 650 °C, which may be ascribed to the drastic component change within the whole NP caused by the excessive interdiffusion (Supplementary Fig. 8). Inspired by this specific evolution of atomic ordering in this multi-component, a further composition analysis is needed clarify the effect of anisotropic Pd atom diffusion.

According to our observation, we hypothesize that the ordering mechanism of Pd@Pt-Co NPs during in-situ continuous heating involves surface activated atoms-assisted nucleation of the intermetallic phase, followed by interdiffusion-facilitated inward propagation of the ordered structure, and the loss of ordered region due to drastic atom diffusion at elevated temperatures. However, to correlate the ordering process with the composition redistribution only based on the structure images captured by in-situ TEM is not possible. Given the composition complexity of this ternary core–shell system, element analysis is required to elucidate the composition change during the ordering process. To address this, ex-situ annealing treatments were performed to replicate the low-temperature ordering transition, followed by atomic resolution element mapping of the annealed NPs.

Correlations between component and ordering conversion

Considering the drastic morphology and core–shell interface change at above 400 °C, it can be referred that the annealing temperature plays a more vital role in maintaining the desired facets compared to the annealing duration, emphasizing the importance of rationally selecting thermal treatment temperature. Therefore, the Pd@Pt-Co cubes were annealed at 400 °C for 5 min under vacuum to verify our hypothesis: the diffusion-manipulated compositional change promotes the surface ordering process occurring at low temperatures. The AC-STEM of ex-situ annealed Pd@Pt-Co is presented in Fig. 4a, revealing the formation of an ordered structure on the surface of well-preserved cubic Pd@Pt-Co core–shell NPs. The ordered structures occupy only a portion of the surface of the NP, which aligns with our observation during in-situ annealing, indicating that the formation of ordered structures predominantly initiates from the surface, albeit with random nucleation sites. To further validate the presence of ordered structure, we enlarged region #1 and constructed an atomic model based on the contrast change within the highlighted laurel-green rectangle (Fig. 4b). The corresponding intensity profile of atomic columns taken along the marked atomic layer reveals a periodic change of alternating intensity peaks (Fig. 4c). Figure 4d–k present the detailed elemental mappings of regions #2 and #3, respectively. Compared to the original elemental distribution (Fig. 1), the Pd exhibits obvious segregation at the surface, along with the inward diffusion of Pt and the ill-defined diffusion of Co. The cyclic voltammetry (CV) tests were also conducted to validate the surface compositional reconstruction. The annealed Pd@Pt-Co sample exhibits a negative shift of hydrogen adsorption/absorption peak in contrast to the original sample and commercial Pt/C (Supplementary Fig. 9), confirming the surface compositional changes caused by the Pd surface segregation^{44,45}. Given the inherent similarity in the face-centered cubic (FCC) structure of Pt and Pd, it could be hypothesized that the outward diffusion of Pd tends to substitute for Pt atoms, contributing to the formation of (Pt, Pd)-Co composition at the surface region. In summary, we believe that the generation of the Ll_2 phase critically depends on the redistribution of composition induced by Pd-diffusion within the nanoscale region.

To further account for the effect of the Pd element on the formation of the intermetallic phase, additional Pt_3Co cubes synthesized

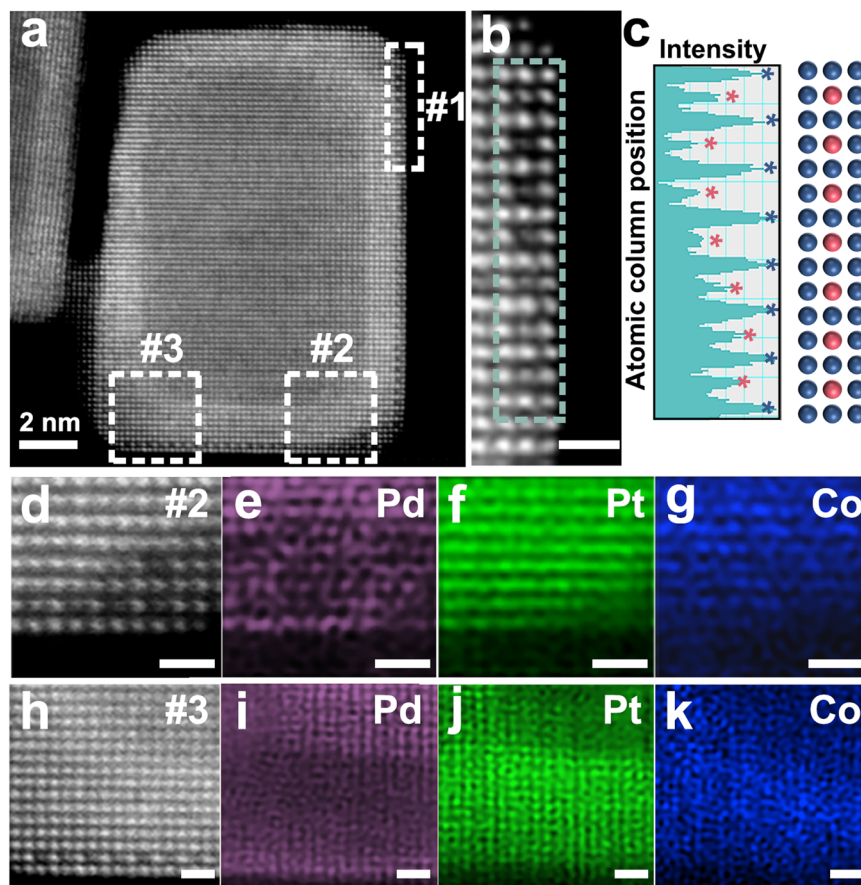


Fig. 4 | Ex-situ structural and composition characterization of Pd@Pt-Co annealing at 400 °C for 5 min. **a**, AC-STEM image of an individual NP at the atomic level. **b**, Enlarged image of region #1 marked by white dotted box (scale bar in **(b)** is 0.5 nm). **c**, Atomic arrangements of the area selected by the laurel-green dashed box, and corresponding intensity profile. **d-g**, Detailed composition analysis at

atomic scales of region #2 (scale bar in **(d, e, f, g)** is 0.5 nm), including HAADF-STEM images **(d)**, EDS elemental maps of Pd **(e)**, Pt **(f)**, and Co **(g)**. **h-k**, Detailed composition analysis at atomic scales of region #3 (scale bar in **(h, i, j, k)** is 0.5 nm), including HAADF-STEM images **(h)**, EDS elemental maps of Pd **(i)**, Pt **(j)**, and Co **(k)**.

using our group's CO-assisted wet-chemical method have been annealed at identical annealing conditions (Supplementary Figs. 10, 11)^{3,34}. The AC-STEM images of Pt₃Co cubes, both before and after annealing, consistently exhibit a uniform contrast distribution, verifying their random alloy structure (Supplementary Figs. 12, 13). Besides, FFT analysis was also performed to investigate the structural discrepancy of surface and core regions. The absence of the (100) and (110) planes in both FFT patterns further corroborates their random solid solution structure (Supplementary Figs. 12, 13). Furthermore, another Pd@Pt-Co NP was annealed at 400 °C for 5 min to provide additional evidence for the feasibility of this annealing regime (Supplementary Fig. 14). The periodical change in Z-contrast observed at the surface region indicates the formation of the intermetallic phase under this condition. In addition, the presence of superlattice spots in the FFT pattern of the surface region and the regular intensity profile for the selected region serve together as compelling evidence of the occurrence of ordering transition. Based on our comprehensive observation, it is evident that the surface Pd-substitution plays a pivotal role in promoting the nucleation and growth of the intermetallic phase in Pd@Pt-Co cubes. This finding emphasizes the significance of Pd as a key contributing factor to the structural evolution and ordered phase formation within the investigated nanomaterial system.

Pd-substitution induces low-temperature phase transition

To gain deeper insights into the underlying mechanism driving the experimentally observed substitution-induced disorder-to-order

transition, density functional theory (DFT) calculations were conducted to theoretically predict the likelihood of low-temperature phase transition in the (Pt, Pd)-Co system. Based on our experimental findings, we constructed two primitive structures to model their random and ordered structure, respectively (Fig. 5a). The reconstructed atomic ratio of Pt and Co was determined by the line profiles derived from EDS analysis (Supplementary Figs. 15, 16). Specifically, both the (Pt, Pd)-Co and Pt-Co ordered systems adopt the L1₂ intermetallic phase. The key difference is that in the (Pt, Pd)-Co ternary system, Pd partially substitutes for Pt at the {0,1/2,1/2} atomic sites, whereas in the Pt-Co system, only Pt occupies these sites. In both systems, Co atoms occupy the (0,0,0) positions (Fig. 5a). Then using a widely reported method to evaluate the critical temperature for phase transition^{46,47}, we found that the T_c of (Pt, Pd)-Co is 362 °C lower than that of the Pt-Co system (Fig. 5b and Supplementary Table 1). Considering the Pt-Co phase diagram, the T_c of Pt₃Co is at approximately 747 °C⁴⁸, whereas the calculated T_c of (Pt, Pd)-Co is predicted to be 385 °C, aligning well with the observed phase transition occurring at about 400 °C. According to the correlation between the ordering kinetics and the diffusivity, higher T_c correlates with lower atom diffusivity^{49,50}. Thus, the reduced T_c of the (Pt, Pd)-Co system suggests the decreased activation energy for atomic diffusion, thus a higher propensity for ordering transition, which allows the formation of an ordered structure at lower annealing temperatures.

As shown in Fig. 5c, the results in our in-situ and ex-situ work can be illustrated using the primary component systems Pd, Pt-Co, and (Pt, Pd)-Co. Given the compositional complexity of this multi-component

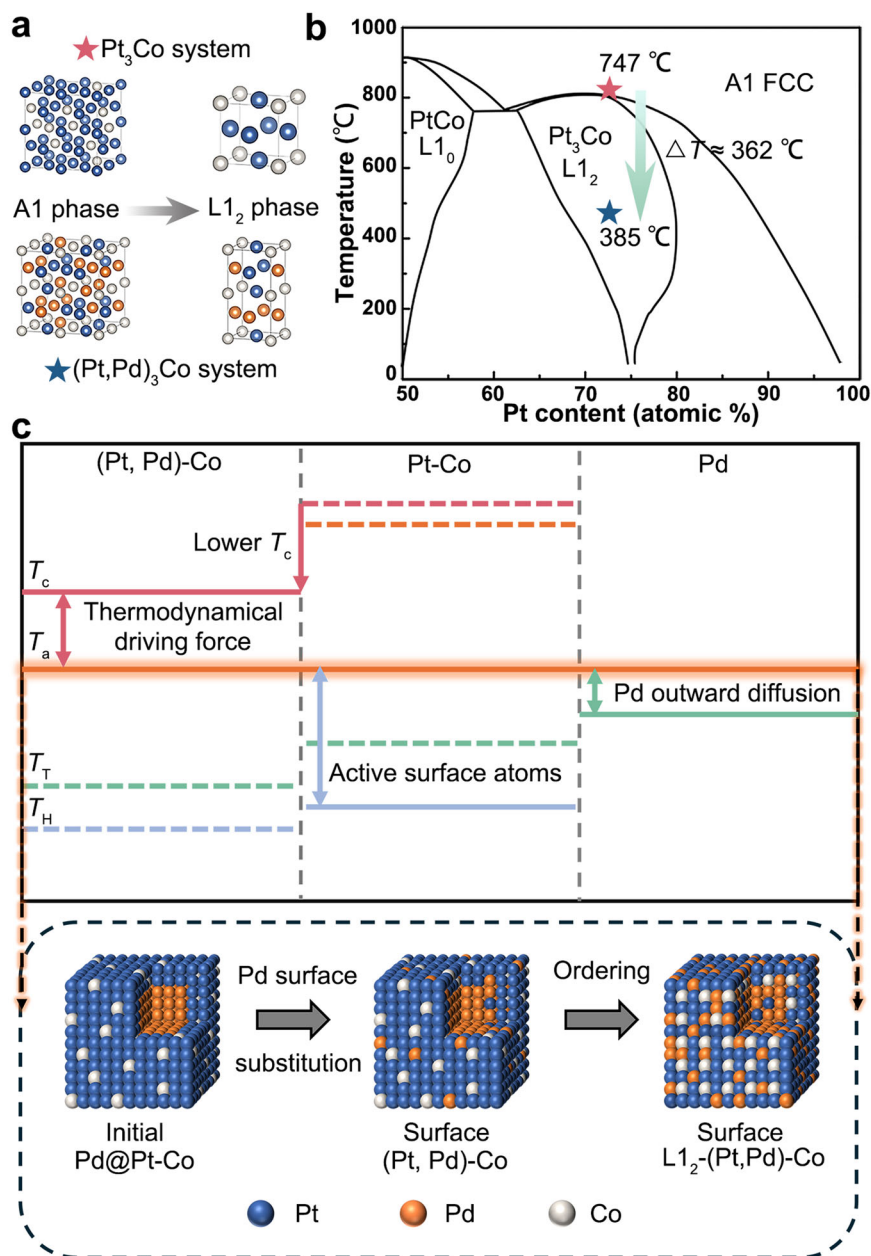


Fig. 5 | The underlying mechanism of low-temperature phase transition.

a, Primitive models of random and ordered structures for Pt-Co and (Pt, Pd)-Co systems. **b**, Calculated temperature for the phase transition process of (Pt, Pd)-Co and Pt-Co system. Pt-Co phase diagram reproduced with permission from ref. 48. Copyright 2004 American Physical Society. **c**, Schematic illustration of the temperature

dependence on the component, and models for the evolution of Pd@Pt-Co cubes annealing at the given annealing temperature (T_a). The pink lines represent the T_c ; The orange line indicates the T_a ; The green lines correspond to the T_T ; The blue lines denote the T_H . The solid-colored lines highlight the temperature thresholds relevant to the experimental results in this study. The dotted-colored lines serve as the references.

system, we qualitatively label the T_T , T_H , and T_c in these components. To ensure the outward diffusion of interior Pd atoms, the T_a should exceed the T_T of Pd. It should also surpass the T_H of Pt-Co, so that the surface Pt-Co atoms are mobile under this condition. Additionally, considering the thermodynamics of ordering conversion, the Gibbs free energy difference between disordered phase and ordered phase becomes negative at temperatures below T_c , providing the thermodynamical driving force for the disorder-to-order transition to occur. In this case, the mobile surface atoms, together with the outward diffusing Pd atoms, promote the substitution of Pt with Pd atoms and the formation of a (Pt, Pd)-Co system, with significantly lower T_c than that of the Pt-Co system. This surface composition change promotes the subsequent ordering process, as depicted in the models for the structural evolution of NPs annealed at T_a . Furthermore, combined

with the in-situ observation, a critical time window also could be predicted, during which the accumulated atomic diffusion is sufficient to promote surface ordering conversion without being so intense as to compromise the desired structure and ordered features. Therefore, atomic migration in a multi-component system plays a pivotal role in modifying the local chemical environment and structure that determines the disorder-to-order phase transition kinetics.

To conclude, we provided a comprehensive understanding of the ordering process in Pd@Pt-Co cubes at low temperatures by combining the detailed in-situ observation and elaborate ex-situ analysis. The atomic diffusion underlying this unexpected low-temperature phase transition mainly consists of two stages: 1) The outward migration and substitution of Pd, in conjunction with surface active atoms, trigger the nucleation of intermetallic by forming (Pt, Pd)-Co system

with a lower T_c ; 2) The moderate interdiffusion of atoms promotes the coalescence and propagation of ordered structures within the NPs. The crucial role of Pd substitution in promoting the disorder-to-order transition is further verified by the DFT calculations, revealing that the formed (Pt, Pd)-Co ternary system exhibits a significant reduction of T_c by approximately 362 °C, compared to the Pt-Co system. Further observations at higher annealing temperatures reveal that the excessive interdiffusion across the interface would lead to the loss of atomic features due to the disruption of stoichiometric ratio, along with the obvious deformation. These findings highlight the significant role of substituted atoms in facilitating the phase transition process at low temperatures. Moreover, they offer insights into the regulation of elemental diffusion behavior, presenting possibilities for controlling the formation of intermetallic phases in complex structures, such as multi-component shape-controlled core-shell NPs.

Methods

Chemicals and Materials

Sodium tetrachloropalladate (II) (Na_2PdCl_4 , 98%), ascorbic acid (AA, $\geq 99.0\%$), potassium chloride (KCl, $\geq 99.5\%$), poly(vinylpyrrolidone) (PVP, $M_w \approx 55,000 \text{ g mol}^{-1}$), potassium bromide (KBr, $\geq 99.0\%$), chloroplatinic acid hexahydrate ($\text{H}_2\text{PtCl}_6 \cdot 6\text{H}_2\text{O}$, Pt $\geq 37.5\%$), 2,4-pentanedione cobalt (2:1) ($\text{Co}(\text{acac})_2$, 97%), *n*-butylamine ($\geq 98\%$), and Nafion (0.5 wt.%) were bought from Sigma-Aldrich. Oleylamine (OAm, 80–90%), oleic acid (OA, 99.7%), and glucose ($\geq 99.5\%$) were purchased from Aladdin. Toluene ($\geq 99.5\%$), ethanol ($\geq 99.7\%$), acetone ($\geq 99.5\%$), chloroform ($\geq 99.0\%$), and formaldehyde (HCHO, 37–40 vol.%) were bought from Sinopharm Chemical Reagent Co., Ltd. Carbon black (C, Vulcan® XC-72R, 20 wt.%) was purchased from Cabot. Deionized water (DI water) used was 18.2 MΩ cm. All chemicals and materials were used as received.

Synthesis of Pd cubes

The Pd cubic seeds with an average size of 10 nm were synthesized based on ref. 13. In a typical synthesis, 105 mg of PVP, 300 mg of KBr, and 60 mg of AA were first dissolved in the 8.0 mL deionized water using a 20-mL glass vial. Then, the mixture was preheated at 80 °C for 8 min. Subsequently, 3 mL of deionized water containing 57 mg of Na_2PdCl_4 was quickly added to the above solution. The reaction was then kept at 80 °C under magnetic stirring for another 3 h. The Pd seeds were collected by centrifugation and washed with ethanol and acetone three times. Finally, the obtained Pd seeds were dispersed in 8 mL of ethanol for further use.

Phase transfer of Pd cubes

According to the previous work, 3 mL of toluene and 5 mL of OAm were mixed with the 8 mL of ethanol containing Pd cubic seeds¹³. Subsequently, the mixture was kept overnight at 80 °C under magnetic stirring. Finally, the product was obtained by centrifugation and washed with chloroform and ethanol three times, then re-dispersed into 11 mL of OAm for the next step.

Synthesis of Pd@Pt-Co cubes

In a typical synthesis, a 1.5 mL OAm solution containing 10 nm Pd cubic seeds and 20 mg glucose was added in 3.5 mL OAm. Firstly, the mixture was preheated at 200 °C for 5 min. Next, 2.5 mL $\text{Co}(\text{acac})_2$ with a concentration of 0.001 mol L^{-1} and 2.5 mL $\text{H}_2\text{PtCl}_6 \cdot 6\text{H}_2\text{O}$ with a concentration of 0.003 mol L^{-1} were slowly injected into the reaction solution via syringe pump at the rate of 0.5 mL h^{-1} . After finishing the injection, the mixture was kept at 200 °C for an extra 30 min. Then, the reaction solution was cooled to RT. The final product was washed 3 times with chloroform and ethanol, then re-dispersed in chloroform.

Synthesis of Pt₃Co cubes

The Pt₃Co cubes were synthesized by a gas-assisted method. In the standard procedure, 20 mg of Pt(acac)₂, 4.4 mg of Co(acac)₂, 9 mL of

OAm, and 1 mL of OA were mixed in a 25 mL three-necked flask³⁴. The Schlenk line was used to control the gas flow during the synthesis. Firstly, the air in the flask was removed by switching the argon and vacuum pump. After that, the flask containing the reaction mixture was placed in an oil bath and preheated at 130 °C for 5 min under argon flow. Then, the gas was changed to carbon monoxide (CO), and the flow rate was set at 190 mL min^{-1} . The mixture under CO flow was transferred to another oil bath and kept at 210 °C for another 40 min. For further use, the reaction mixture was centrifugated and washed with ethanol and chloroform three times.

Preparation of carbon-supported catalyst

The obtained Pd@Pt-Co and Pt₃Co NPs were mixed with carbon black (Vulcan XC 72 R) with a mass ratio of 1:4 (metal: carbon)¹³. Firstly, a certain amount of carbon support was sonicated in chloroform for 1 h, followed by the addition of metal catalysts and another 30 min of ultrasonic treatment. The carbon-support products were obtained by centrifugating and drying under Argon flow. Subsequently, the catalysts were re-dispersed in *n*-butylamine and stirred for 3 days to clean the surface of the catalyst. By centrifugated and washed with methanol at $5,000 \times g$ for 5 min, the catalysts were isolated from the mixture. Finally, the carbon-supported catalysts were dried through a freeze dryer under a vacuum to obtain a loose structure.

Ex-situ thermal treatment of catalysts

The carbon-support catalysts were placed in a quartz boat and loaded in a tube furnace. The furnace was connected to a pressure indicator and a vacuum pump. The quartz boat containing the catalyst sample was pulled to the center of the furnace when the temperature achieved 400 °C and kept at this site for 5 min. After completing the annealing treatment, the quartz boat was quickly dragged to the other end of the furnace for rapid cooling.

Electrochemical test

The electrochemical test was carried out using a typical three-electrode cell on the CHI760E station. The Pt filament was utilized as the counter electrode, the reversible hydrogen electrode (RHE) was employed as the reference electrode, and the glassy-carbon (GC) rotating disk electrode with an area of 0.196 cm^2 served as the working electrode. To prepare the catalyst ink, 5 mg of catalysts were mixed with 1 mL isopropanol, 4 mL DI water, and 25 μL Nafion. The resulting solution was carefully dropped onto the surface of the GC electrode. CV curves were obtained by scanning in the range of 0.05 to 1.0 V (vs. RHE) in an Ar-saturated 0.1 M HClO₄ solution at a rate of 50 mV s^{-1} .

Materials characterization

Transmission electron microscopy (TEM) images and energy dispersive X-ray (EDX) spectra were taken on the JEOL JEM-2100F operated at 200 kV. High-angle annular dark-field scanning TEM (HAADF-STEM) and EDX mapping analyses were performed on the Talos F200X G2 operated at 200 kV. The aberration-corrected STEM(AC-TEM) images were taken on the JEM-ARM300F microscope equipped with dual spherical aberration correctors at an accelerating voltage of 300 kV.

In-situ STEM characterization

The Pd@Pt-Co NPs dispersed in chloroform were dropped onto the Fusion Thermal E-chips. The E-chip was then mounted onto the Fusion heating holder (Protochips). The in-situ holder was inserted into the JEM-ARM 300 F equipped with dual spherical aberration correctors, operating at an accelerating voltage of 300 kV. The Fusion holder allowed for precise temperature control during specimen annealing. In one experiment, the specimen was heated from room temperature to 400 °C rapidly and held at 400 °C for further observations (see Suppl. Movie 1). It is noted that the electron beam was blanked during the

temperature ramp and stabilization to minimize its effect on the specimen. The initiation of video recording was set as $t = 0$ s. For the second observation, the sample was heated from 445 to 470 °C at a ramping rate of 2.5 °C min⁻¹ (see Suppl. Movie 2).

QSTEM image simulation

The simulated HAADF-STEM images of core-shell NPs with random surface and L1₂ ordered surface along [001] zone axis are presented in Fig. 2d, h, respectively. The multi-slice simulation for the core-shell NPs was conducted using a voltage of 300 kV, a convergence angle of 19.3 mrad, and inner- and outer collection angles of 70 and 200 mrad by QSTEM software. In the simulated HAADF-STEM images, the contrast variation reflects the atomic arrangements, which can be attributed to the different Z values of elements comprising the Pd@Pt-Co NPs. To provide further insights into the simulation process, Supplementary Figs. 4, 5 show the simulated image sequences for Pd@Pt-Co and in-situ annealed Pd@Pt-Co, respectively, with different slice thicknesses.

First-principles calculations

We performed all calculations using the Vienna ab-initio Simulation Package (VASP). We treated exchange-correlation with the Generalized Gradient Approximation (GGA), as parameterized by Perdew, Burke, and Ernzerhof (PBE), using the potentials supplied by VASP with the projected augmented wave (PAW) method. To simulate the ordered phases of Pt₃Co and (Pt, Pd)₃Co, cluster expansion searching was conducted by the Alloy Theoretic Automated Toolkit (ATAT) package with the most stable substituted forms obtained. To model the disordered phases, the Special Quasi-random Structures (SQS) method was used with 32 site cubic supercells with Pt/Pd occupying the 24 sites in a 1:1 ratio. The SQS was generated using a Monte Carlo algorithm as implemented in the ATAT package with the pair and triplet correlation functions of the SQS constrained to be identical to those of the statistically random compound. The Brillouin zone was sampled by 12 × 12 × 12 and 7 × 7 × 7 Gamma centered mesh for the ordered and disordered cells, respectively, after a convergence test. Electronic ground states were converged to within 1 × 10⁻⁸ eV atom⁻¹, and forces were converged to less than 0.02 eV Å⁻¹.

Calculation details of phase transition temperature change ΔT_c

To estimate the energetic influence of the Pd elemental substitution on the phase transition between ordered and disordered phases, the resulting change of the phase transition temperature ΔT_c can be computed. As shown in equation (1), ΔT_c is calculated through dividing the enthalpy difference between random and ordered phases by the ideal configurational entropy following refs. 46,47:

$$\Delta T_c \approx \frac{E^{\text{SQS}}(\text{Pt}_3\text{Co}) - E^{\text{L1}_2}(\text{Pt}_3\text{Co})}{\Delta S_{\text{ideal}}(\text{Pt}_3\text{Co})} - \frac{E^{\text{SQS}}((\text{Pt}, \text{Pd})_3\text{Co}) - E^{\text{L1}_2}((\text{Pt}, \text{Pd})_3\text{Co})}{\Delta S_{\text{ideal}}((\text{Pt}, \text{Pd})_3\text{Co})} \quad (1)$$

E^{SQS} and E^{L1_2} are the enthalpies of random and ordered phases, respectively. The ΔS_{ideal} is the ideal configurational entropy, which can be calculated according to the following formula:

$$\Delta S_{\text{ideal}} = -R \sum X_m \ln X_m \quad (2)$$

The R is the ideal gas constant, 8.63 × 10⁻⁵ eV K⁻¹ atom⁻¹. The X_m is the concentration of elements in the system. It is worth mentioning that the obtained ideal configurational entropy also needs to be normalized per atom to match the formation energy values, which are represented by $E_{\text{form}}^{\text{SQS}}$ and $E_{\text{form}}^{\text{L1}_2}$, respectively. Specifically speaking, the (Pt, Pd)₃-Co system exhibits a notable entropy gain and decreased free energy gap against the Pt-Co system, thus leading to a lowered phase transition temperature. The specific calculated values are listed in Supplementary Table 1.

Reporting summary

Further information on research design is available in the Nature Portfolio Reporting Summary linked to this article.

Data availability

The data that support the findings of this study are available from the corresponding authors upon request. Source data are provided with this paper.

References

- Greeley, J. et al. Alloys of platinum and early transition metals as oxygen reduction electrocatalysts. *Nat. Chem.* **1**, 552–556 (2009).
- Chen, A. & Holt-Hindle, P. Platinum-based nanostructured materials: synthesis, properties, and applications. *Chem. Rev.* **110**, 3767–3804 (2010).
- Wu, J. & Yang, H. Platinum-based oxygen reduction electrocatalysts. *Acc. Chem. Res.* **46**, 1848–1857 (2013).
- Zhou, M., Li, C. & Fang, J. Noble-metal based random alloy and intermetallic nanocrystals: syntheses and applications. *Chem. Rev.* **121**, 736–795 (2021).
- Wang, D. et al. Structurally ordered intermetallic platinum-cobalt core-shell nanoparticles with enhanced activity and stability as oxygen reduction electrocatalysts. *Nat. Mater.* **12**, 81–87 (2013).
- Wang, Y. et al. Carbon-supported Pt-based alloy electrocatalysts for the oxygen reduction reaction in polymer electrolyte membrane fuel cells: particle size, shape, and composition manipulation and their impact to activity. *Chem. Rev.* **115**, 3433–3467 (2015).
- Seh, Z. et al. Combining theory and experiment in electrocatalysis: insights into materials design. *Science* **355**, eaad4998 (2017).
- Liu, M., Zhao, Z., Duan, X. & Huang, Y. Nanoscale Structure Design for High-Performance Pt-Based ORR Catalysts. *Adv. Mater.* **31**, e1802234 (2019).
- Stamenkovic, V. R. et al. Improved oxygen reduction activity on Pt₃Ni(111) via increased surface site availability. *Science* **315**, 493–497 (2007).
- Ryu, J. et al. Morphology-controlled synthesis of ternary Pt-Pd-Cu alloy nanoparticles for efficient electrocatalytic oxygen reduction reactions. *Appl. Catal. B-Environ.* **174**, 526–532 (2015).
- Zhao, X. et al. Multiple metal-nitrogen bonds synergistically boosting the activity and durability of high-entropy alloy electrocatalysts. *J. Am. Chem. Soc.* **146**, 3010–3022 (2024).
- Zhao, X. et al. Octahedral Pd@Pt_{1.8}Ni core-shell nanocrystals with ultrathin PtNi alloy shells as active catalysts for oxygen reduction reaction. *J. Am. Chem. Soc.* **137**, 2804–2807 (2015).
- Shi, F. et al. Design of highly durable core-shell catalysts by controlling shell distribution guided by in-situ corrosion study. *Adv. Mater.* **33**, e2101511 (2021).
- Porter, N. S., Wu, H., Quan, Z. & Fang, J. Shape-control and electrocatalytic activity-enhancement of Pt-based bimetallic nanocrystals. *Acc. Chem. Res.* **46**, 1867–1877 (2013).
- Lee, Y.-W. et al. Pd@Pt core-shell nanostructures for improved electrocatalytic activity in methanol oxidation reaction. *Appl. Catal. B-Environ.* **179**, 178–184 (2015).
- Shan, H. et al. Nanoscale kinetics of asymmetrical corrosion in core-shell nanoparticles. *Nat. Commun.* **9**, e1011 (2018).
- Shi, F. et al. Strain-induced corrosion kinetics at nanoscale are revealed in liquid: enabling control of corrosion dynamics of electrocatalysis. *Chem.* **6**, 2257–2271 (2020).
- Yan, Y. et al. Intermetallic nanocrystals: syntheses and catalytic applications. *Adv. Mater.* **29**, e1605997 (2017).
- Cui, M. et al. Multi-principal elemental intermetallic nanoparticles synthesized via a disorder-to-order transition. *Sci. Adv.* **8**, eabm4322 (2022).

20. Xiong, Y. et al. Revealing the atomic ordering of binary intermetallics using in situ heating techniques at multilength scales. *Proc. Natl. Acad. Sci. USA* **116**, 1974–1983 (2019).
21. Yang, C. et al. Sulfur-anchoring synthesis of platinum intermetallic nanoparticle catalysts for fuel cells. *Science* **374**, 459–464 (2021).
22. Chi, M. et al. Surface faceting and elemental diffusion behaviour at atomic scale for alloy nanoparticles during in situ annealing. *Nat. Commun.* **6**, e8925 (2015).
23. Zhao, T. et al. Self-optimized ligand effect in L1₂-PtPdFe intermetallic for efficient and stable alkaline hydrogen oxidation reaction. *ACS Catal.* **10**, 15207–15216 (2020).
24. Nakaya, Y. et al. High-entropy intermetallics serve ultrastable single-atom Pt for propane dehydrogenation. *J. Am. Chem. Soc.* **144**, 15944–15953 (2022).
25. Vara, M. et al. Understanding the thermal stability of palladium–platinum core–shell nanocrystals by in situ transmission electron microscopy and density functional theory. *ACS Nano* **11**, 4571–4581 (2017).
26. Bonifacio, C. S. et al. Thermal stability of core-shell nanoparticles: a combined in situ study by XPS and TEM. *Chem. Mater.* **27**, 6960–6968 (2015).
27. Huang, R., Wen, Y., Zhu, Z. & Sun, S. Pt-Pd Bimetallic Catalysts: Structural and Thermal Stabilities of Core-Shell and Alloyed Nanoparticles. *J. Phys. Chem. C* **116**, 8664–8671 (2012).
28. Aso, K. et al. Singular behaviour of atomic ordering in Pt-Co nanocubes starting from core-shell configurations. *Nanoscale* **14**, 9842–9848 (2022).
29. Pan, Y. & Yang, H. Design of bimetallic catalysts and electrocatalysts through the control of reactive environments. *Nano Today* **31**, e100832 (2020).
30. Vitos, L., Ruban, A. V., Skriver, H. L. & Kollar, J. The surface energy of metals. *Surf. Sci.* **411**, 186–202 (1998).
31. Dai, S. et al. In situ atomic-scale observation of oxygen-driven core-shell formation in Pt₃Co nanoparticles. *Nat. Commun.* **8**, e204 (2017).
32. Ma, T. et al. Toward phase and catalysis control: tracking the formation of intermetallic nanoparticles at atomic scale. *Chem* **5**, 1235–1247 (2019).
33. Dai, S. et al. Revealing surface elemental composition and dynamic processes involved in facet-dependent oxidation of Pt₃Co nanoparticles via in situ transmission electron microscopy. *Nano Lett.* **17**, 4683–4688 (2017).
34. Li, F. et al. Atomistic imaging of competition between surface diffusion and phase transition during the intermetallic formation of faceted particles. *ACS Nano* **15**, 5284–5293 (2021).
35. Chen, X. et al. Composition-dependent ordering transformations in Pt-Fe nanoalloys. *Proc. Natl. Acad. Sci. USA* **119**, e2117899119 (2022).
36. Zeng, W. et al. Phase diagrams guide synthesis of highly ordered intermetallic electrocatalysts: separating alloying and ordering stages. *Nat. Commun.* **13**, 7654–7654 (2022).
37. Dai, Y. et al. The physical chemistry and materials science behind sinter-resistant catalysts. *Chem. Soc. Rev.* **47**, 4314–4331 (2018).
38. Prieto, G. et al. Hollow nano- and microstructures as catalysts. *Chem. Rev.* **116**, 14056–14119 (2016).
39. Wolf, M., Kotze, H., Fischer, N. & Claeys, M. Size dependent stability of cobalt nanoparticles on silica under high conversion Fischer-Tropsch environment. *Faraday Discuss.* **197**, 243–268 (2017).
40. Lee, J., Tanaka, T., Lee, J. & Mori, H. Effect of substrates on the melting temperature of gold nanoparticles. *Calphad* **31**, 105–111 (2007).
41. Yu, S. & Yang, H. Design principles for the synthesis of platinum-cobalt intermetallic nanoparticles for electrocatalytic applications. *Chem. Commun.* **59**, 4852–4871 (2023).
42. Castro, T., Reifemberger, R., Choi, E. & Andres, R. P. Size-dependent melting temperature of individual nanometer-sized metallic clusters. *Phys. Rev. B* **42**, 8548–8556 (1990).
43. Song, T. et al. Small molecule-assisted synthesis of carbon supported platinum intermetallic fuel cell catalysts. *Nat. Commun.* **13**, e6521 (2022).
44. Lu, Y. & Chen, W. PdAg alloy nanowires: facile one-step synthesis and high electrocatalytic activity for formic acid oxidation. *ACS Catal.* **2**, 84–90 (2012).
45. Chen, Y. et al. Core-shell CuPd@Pd tetrahedra with concave structures and Pd-enriched surface boost formic acid oxidation. *J. Mater. Chem. A* **6**, 10632–10638 (2018).
46. Jia, Y., Shu, X., Xie, Y. & Chen, Z. Physical properties of FePt nanocomposite doped with Ag atoms: first-principles study. *Chin. Phys. B* **23**, e076105 (2014).
47. Hu, C. et al. From symmetry to entropy: crystal entropy difference strongly affects early stage phase transformation. *Appl. Phys. Lett.* **115**, e264103 (2019).
48. Mehaddene, T. et al. Lattice dynamics and migration enthalpies in CoPt₃ and FePd. *Phys. Rev. B* **69**, e024304 (2004).
49. Cahn, Robert W. Ordering kinetics and diffusion in some L1₂ alloys. *MRS OPL* **57**, 385 (1985).
50. Liang, J. et al. Metal bond strength regulation enables large-scale synthesis of intermetallic nanocrystals for practical fuel cells. *Nat. Mater.* **23**, 1259–1267 (2024).

Acknowledgements

This work was sponsored by National Key R&D Program of China (No. 2017YFB0406000), the National Natural Science Foundation of China (21875137, 51521004, and 51420105009), Program of Shanghai Academic/Technology Research Leader (Project No. 23XD1422100), and the Innovation Program of Shanghai Municipal Education Commission (Project No. 2019-01-07-00-02-E00069), the 111 Project (Project No. B16032), and the support from Center of Hydrogen Science and Joint Research Center for Clean Energy Materials from Shanghai Jiao Tong University.

Author contributions

W.Z., F.L., and J.W. conceived the idea and designed the experiments. F.L. and D.W. carried out the electron transmission microscopy characterization. W.Z. performed electrochemical measurements and compositional analysis. W.Z., Y.L., Z.Y. and J.W. designed and implemented the DFT calculations. W.Z., K.Y., W.G., and J.W. processed the in-situ data and analyzed the results. W.Z., A.S., W.G., and J.W. discussed and proposed the mechanism. W.Z. and J.W. wrote the manuscript and organized the supplementary information. W. S., Z.Y., W.G., and T.D. revised the manuscript. All the authors contributed to the discussions.

Competing interests

The authors declare no competing interests.

Additional information

Supplementary information The online version contains supplementary material available at <https://doi.org/10.1038/s41467-024-54104-5>.

Correspondence and requests for materials should be addressed to Zhenpeng Yao, Wenpei Gao or Jianbo Wu.

Peer review information *Nature Communications* thanks Guangwen Zhou who co-reviewed with Xiaobo Chen and the other, anonymous, reviewers for their contribution to the peer review of this work. A peer review file is available.

Reprints and permissions information is available at <http://www.nature.com/reprints>

Publisher's note Springer Nature remains neutral with regard to jurisdictional claims in published maps and institutional affiliations.

Open Access This article is licensed under a Creative Commons Attribution-NonCommercial-NoDerivatives 4.0 International License, which permits any non-commercial use, sharing, distribution and reproduction in any medium or format, as long as you give appropriate credit to the original author(s) and the source, provide a link to the Creative Commons licence, and indicate if you modified the licensed material. You do not have permission under this licence to share adapted material derived from this article or parts of it. The images or other third party material in this article are included in the article's Creative Commons licence, unless indicated otherwise in a credit line to the material. If material is not included in the article's Creative Commons licence and your intended use is not permitted by statutory regulation or exceeds the permitted use, you will need to obtain permission directly from the copyright holder. To view a copy of this licence, visit <http://creativecommons.org/licenses/by-nc-nd/4.0/>.

© The Author(s) 2024